15 Apr 2022

Building-Block Approach to the Discovery of Na8Mn2(Ge2Se6)2: A Polar Chalcogenide Exhibiting Promising Harmonic Generation Signals with a High Laser-Induced Damage Threshold

Srikanth Balijapelly

Andrew J. Craig

Jeong Bin Cho

Joon I. Jang

et. al. For a complete list of authors, see https://scholarsmine.mst.edu/phys_facwork/2246

Recommended Citation

S. Balijapelly et al., "Building-Block Approach to the Discovery of Na8Mn2(Ge2Se6)2: A Polar Chalcogenide Exhibiting Promising Harmonic Generation Signals with a High Laser-Induced Damage Threshold," *Journal of Alloys and Compounds*, vol. 900, article no. 163392, Elsevier, Apr 2022.
The definitive version is available at https://doi.org/10.1016/j.jallcom.2021.163392

Journal of Alloys and Compounds 900 (2022) 163392

Contents lists available at ScienceDirect

Journal of Alloys and Compounds

journal homepage: www.elsevier.com/locate/jalcom

Building-block approach to the discovery of $Na_8Mn_2(Ge_2Se_6)_2$: A polar chalcogenide exhibiting promising harmonic generation signals with a high laser-induced damage threshold

Srikanth Balijapelly[a], Andrew J. Craig[b], Jeong Bin Cho[c], Joon I. Jang[c,*], Kartik Ghosh[d], Jennifer A. Aitken[b], Aleksandr V. Chernatynskiy[e], Amitava Choudhury[a,*]

[a] Department of Chemistry, Missouri University of Science and Technology, Rolla, MO 65409, USA
[b] Department of Chemistry and Biochemistry, Duquesne University, Pittsburgh, PA 15282, USA
[c] Department of Physics, Sogang University, 35 Baekbeom-ro, Mapo-gu, Seoul 04107, South Korea
[d] Department of Physics, Astronomy and Materials Sci, Missouri State University, 901S. National Ave., Springfield, MO 65897, USA
[e] Department of Physics, Missouri University of Science and Technology, Rolla, MO 65409, USA

ARTICLE INFO

Article history:
Received 6 October 2021
Received in revised form 14 December 2021
Accepted 20 December 2021
Available online 23 December 2021

Keywords:
NLO
SHG
THG
Polar crystal
High LIDT
Chalcogenides

ABSTRACT

A new polar quaternary chalcogenide, $Na_8Mn_2(Ge_2Se_6)_2$, has been synthesized using the building-block approach by reacting preformed $Na_6Ge_2Se_6$ and $MnCl_2$ at 750 °C. The structure consists of layers of $[Na(1)Mn(Ge_2Se_6)]^{3-}$ stacked perpendicular to the *c*-axis and sodium ions occupying the interlayer space. An indirect bandgap of 1.52 eV has been calculated using density functional theory, which is expectedly underestimated compared to the observed optical bandgap of 1.95 eV derived from diffuse reflectance spectroscopic measurements in the UV/Vis/NIR region. Magnetic measurements confirm the paramagnetic nature of $Na_8Mn_2(Ge_2Se_6)_2$ with an experimental magnetic moment of 5.8 μ_B in good agreement with the theoretical spin only moment of 5.92 μ_B for high spin Mn^{2+}. $Na_8Mn_2(Ge_2Se_6)_2$ exhibits a potentially wide region of transparency in the measured range of 2.5–25 μm. $Na_8Mn_2(Ge_2Se_6)_2$ shows a modest second-harmonic generation (SHG) response but with a high laser-induced damage threshold (LIDT) of ~9x $AgGaSe_2$. Third harmonic generation (THG) measurements indicate that $Na_8Mn_2(Ge_2Se_6)_2$ displays a high THG coefficient (1.9x $AgGaSe_2$) at λ = 1800 nm.

1. Introduction

Second-order nonlinear optical (NLO) materials that produce a coherent beam in the infrared (IR) region find many applications in telecommunications, IR remote sensing, and minimally-invasive medical surgery [1–4]. On the other hand, third-order NLO materials that exhibit third harmonic generation (THG), the frequency tripling process, are less explored compared to second-order NLO materials. THG materials can be used in several optoelectronic applications [5–7]. While a noncentrosymmetric (NCS) structure is a prerequisite to show second-harmonic generation (SHG), it is not necessary for achieving THG. NCS quaternary chalcogenides with wide bandgaps are perceived as promising NLO materials in the IR region of the electromagnetic spectrum due to their exceptional transparency and optimum bandgap compared to oxides [1–3]. A better understanding and control of the synthetic methodology of chalcogenides has unlocked several promising NLO candidates in the past decade for example, $LiGaGe_2Q_6$ [8], $A_2In_2MQ_6$(*M* = Si, Ge; *Q* = S, Se) [9], Li_2CdGeS_4 [10,11], Li_2MnGeS_4 [12], $Na_4Mg M_2Se_6$ [13], Na_2BaMQ_4 [14], $AgZnPS_4$ and $LiZnPS_4$ [15], α-Li_2ZnGeS_4 [16], and $Li_4MgGe_2S_7$ [17]. Among several main-group chalcometallate compositions, chalcogermanates are unique because of their ability to form various building blocks such as isolated ($[GeQ_4]^{4-}$) [18], corner-shared ($[Ge_2Q_7]^{6-}$) [19], and edge-shared ($[Ge_2Q_6]^{4-}$) [20] tetrahedral units where Ge is formally in +4 oxidation state. On the other hand, there exist Ge–Ge bond containing building units where Ge is formally in +3 oxidation state as in the ethane-like building units, $[Ge_2Q_6]^{6-}$ [21,22] and $[Ge_4Q_{10}]^{8-}$ [22]. Depending on the mode of connectivity between these building units and the other metal ions, M^{n+}, where *M* can be a rare earth, main group, or transition metal, different structure types can be formed [12,13,16,23–28]. Though several

Abbreviations: NLO, Nonlinear Optical; LIDT, Laser-Induced Damage Threshold; SHG, Second Harmonic Generation; TGH, Third Harmonic Generation

* Corresponding authors.
E-mail addresses: jjcoupling@sogang.ac.kr (J.I. Jang), choudhurya@mst.edu (A. Choudhury).

https://doi.org/10.1016/j.jallcom.2021.163392
0925-8388/

compounds exist containing ethane-like chalcogermanate building units [13,23,24,28,29], only $Na_4MgGe_2Se_6$ crystallizes in an NCS space group [13]. To the best of our knowledge, no transition metal analogue of the $Na_4MgGe_2Se_6$ structure-type has been reported thus far, especially with the first row M^{2+} transition metals (M = Mn, Fe, Co, Ni). Hence, we sought to synthesize new NCS compounds containing ethane-like building units and a transition metal. Towards this approach, we have employed the solid-state metathesis route by reacting preformed $Na_6Ge_2Se_6$, which contains ethane-like building units, and $MnCl_2$. This strategy proved successful, as we have isolated $Na_8Mn_2(Ge_2Se_6)_2$, which crystallizes in the polar, NCS space group $C2$. In this article, we report the synthesis, crystal structure, calculated electronic structure, and magnetic properties of $Na_8Mn_2(Ge_2Se_6)_2$ along with its linear and nonlinear optical properties, which make it an attractive new NLO candidate material.

2. Materials and methods

2.1. Synthesis

$Na_8Mn_2(Ge_2Se_6)_2$ was synthesized using the metathesis route by reacting $Na_6Ge_2Se_6$ and $MnCl_2$. First, $Na_6Ge_2Se_6$ was prepared by combining a stoichiometric composition of elements; 3 mmol of Na (Sigma, 99.9%), 1 mmol of Ge (Acros Organics, 99.9%) and 3 mmol of Se (Acros Organics, 99.5%) were heated in a sealed carbon-coated quartz ampoule. The sealed tube was heated to 800 °C at a rate of 45 °C/h, held at that temperature for 2 h and subsequently cooled to room temperature at a rate of 45 °C/h. Greenish-yellow-colored chunks of $Na_6Ge_2Se_6$ were recovered after breaking the ampoule inside an argon-filled glove box. The crystals were found to be air and moisture sensitive. The bulk purity of $Na_6Ge_2Se_6$ was confirmed from laboratory-grade powder X-ray diffraction. $Na_6Ge_2Se_6$ and $MnCl_2$ (1:1) were hand ground together for 15 min and the mixture was loaded into a carbon-coated quartz ampoule. The sealed quartz ampoule was heated to 750 °C at a rate of 25 °C/h and held for 96 h followed by cooling to room temperature at a rate of 35 °C/h. Orange color crystals were recovered after breaking the ampoule in air followed by washing with 10% water in *N, N* dimethylformamide (DMF) solution to remove the NaCl byproduct and to loosen the crystals. A representative digital photograph showing DMF-washed crystals is provided in Fig. S1 (Supplementary Material). The crystals were found to be reasonably stable for several hours under ambient conditions. $Na_8Mn_2(Ge_2Se_6)_2$ was also prepared by reacting a stoichiometric combination of elements; 4 mmol of Na, 1 mmol of Mn, 2 mmol of Ge and 6 mmol of Se were heated in a sealed quartz tube. The temperature of the furnace was raised to 600 °C at a rate of 20 °C/h and held for 96 h followed by cooling to room temperature at a rate of 30 °C/h. An appropriate crystal from the DMF-washed product obtained from metathesis reaction was used for single crystal X-ray diffraction.

2.2. X-ray crystallography

A good-quality crystal was chosen for single crystal X-ray diffraction data collection on a Bruker Smart Apex CCD X-ray diffractometer equipped with a sealed tube X-ray source with Mo Kα radiation (λ = 0.71073 Å). Low-temperature data sets were collected at −53 °C with a step size of 0.3° in the ω scan and 20 s/frame exposure time using SMART [30] software. Data integration and absorption correction were done using the programs SAINT [31] and SADABS [31], respectively. SHELXS-97 [32] and difference Fourier syntheses were used to solve the crystal structures. Full-matrix least-squares refinement against $|F^2|$ was carried out using the SHELXTL-PLUS [32] suite of programs. Final refinements including the anisotropic thermal parameters were carried out using SHELX-2018 with the ShelXle graphical user interface [33]. The compound crystallizes in polar, NCS space group $C2$ (No. 5). Four sodium, three selenium, one germanium and one manganese were easily located from a difference Fourier map and refined isotropically with acceptable thermal displacement parameters. Taking into account the occupancies of each element, a charge balanced formula of $Na_8Mn_2(Ge_2Se_6)_2$ was obtained (Z = 1). It should be noted that in order to be consistent with the previously reported compounds of the general formula $Na_{12-nx}M'_x{}^{n+}(M_2Q_6)_2$ (M = Si, Ge; M' = Eu^{2+}, La^{3+}, Sm^{3+}, Pb^{2+}, Sn^{2+}; Q = S, Se), [23,24,28,29] a formula of $Na_8Mn_2(Ge_2Se_6)_2$ (Z = 1) has been used here instead of $Na_4MnGe_2Se_6$ (Z = 2). Selected crystallographic data and structure refinement details are provided in Table 1. Selected bond lengths are listed in Table 2. Fractional atomic coordinates along with the corresponding isotropic and anisotropic displacement parameters are provided in Tables S1 and S2, respectively (Supplementary Materials). The CIF file has been submitted to CCDC (CSD 2126428) and can be obtained free of charge from The Cambridge Crystallographic Data Centre via www.ccdc.cam.ac.uk/data_request/cif.

Table 1
Selected crystallographic data and refinement details for $Na_8Mn_2(Ge_2Se_6)_2$.

Empirical formula	$Na_8Mn_2Ge_4Se_{12}$
Formula weight	1531.68 g/mol
Temperature	220(2) K
Wavelength	0.71073 Å
Crystal system	Monoclinic
Space group	$C2$
Unit cell dimensions	a = 7.727(4) Å
	b = 11.943(7) Å
	c = 7.085(4) Å
	β = 106.682(6)°
Volume	626.4(6) Å^3
Z	1
Density (calculated)	4.061 Mgm^{-3}
Absorption coefficient	23.278 mm^{-1}
Goodness-of-fit on F^2	1.059
R_1 [$I > 2\sigma(I)$][a]	0.0339
wR_2 (F^2) (all data)[b]	0.0790
Absolute structure parameter	0.48(6)
Largest diff. peak and hole	2.021 and − 1.234 e.Å^{-3}

[a] $R_1 = \sum||F_o| - |F_c|/\sum|F_o|$
[b] $wR_2 = \{\sum[w(F_o^2 - F_c^2)^2]/\sum[w(F_0^2)^2]\}^{1/2}$, $w = 1/[\sigma^2(F_o)^2 + (aP)^2 + bP]$, where $P = [F_o^2 + 2F_c^2]/3$

Table 2
Selected bond lengths of $Na_8Mn_2(Ge_2Se_6)_2$.

Bond	d (Å)	Bond	d (Å)
Mn1 – Se1$^{\#1}$	2.767(3)	Na2 – Se2$^{\#6}$	3.032(6)
Mn1 – Se1$^{\#2}$	2.767(3)	Na2 – Se1$^{\#7}$	3.106(6)
Mn1 – Se2$^{\#3}$	2.826(3)	Na2 – Se1$^{\#5}$	3.106(6)
Mn1 – Se2	2.826(3)	Na2 – Se3	3.120(3)
Mn1 – Se3$^{\#5}$	2.837(2)	Na2 – Se3$^{\#8}$	3.120(3)
Mn1 – Se3	2.837(2)	Na3 – Se1	2.960(2)
Ge1 – Se3	2.345(2)	Na3 – Se1$^{\#8}$	2.960(2)
Ge1 – Se2	2.344(3)	Na3 – Se2$^{\#6}$	3.089(5)
Ge1 – Se1	2.364(3)	Na3 – Se2$^{\#4}$	3.089(5)
Ge1 – Ge1$^{\#4}$	2.402(2)	Na3 – Se3$^{\#9}$	3.127(6)
Na1 – Se3	2.990(5)	Na3 – Se3$^{\#10}$	3.127(6)
Na1 – Se3$^{\#4}$	2.990(5)	Na4 – Se3$^{\#11}$	2.932(6)
Na1 – Se1$^{\#2}$	3.006(2)	Na4 – Se3	2.932(6)
Na1 – Se1$^{\#5}$	3.006(2)	Na4 – Se1	3.006(6)
Na1 – Se2$^{\#2}$	3.064(6)	Na4 – Se1$^{\#11}$	3.006(6)
Na1 – Se2$^{\#5}$	3.064(6)	Na4 – Se2$^{\#3}$	3.023(2)
Na2 – Se2$^{\#4}$	3.032(6)	Na4 – Se2$^{\#6}$	3.023(2)

Symmetry transformations used to generate equivalent atoms:
$^{\#1}$ x, y, z-1; $^{\#2}$ x + 1/2, y + 1/2, z; $^{\#3}$ -x, y, -z; $^{\#4}$ x-1/2, y-1/2, z; $^{\#5}$ x-1/2, y + 1/2, z; $^{\#6}$ -x + 1/2, y + 1/2, -z; $^{\#7}$ -x + 1, y, -z; $^{\#8}$ x, y, z + 1; $^{\#9}$ -x + 1/2, y + 1/2, -z + 1; $^{\#10}$ -x, y, -z + 1; $^{\#11}$ -x + 1, y, -z + 1.

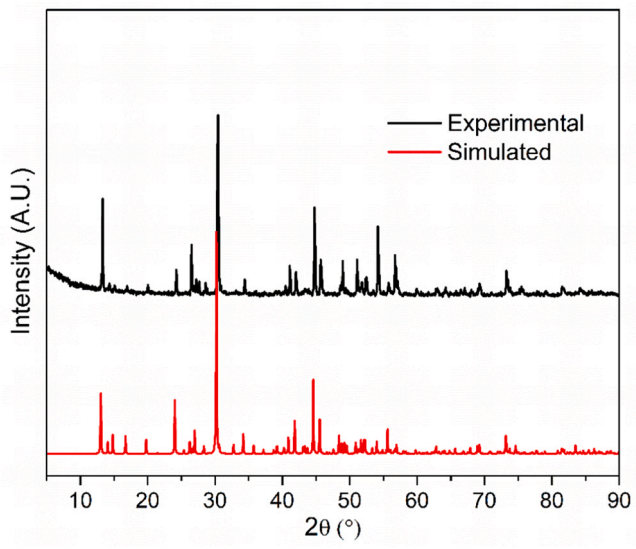

Fig. 1. Comparison of simulated and experimental PXRD patterns of DMF washed $Na_8Mn_2(Ge_2Se_6)_2$ synthesized from solid-state metathesis reaction ($Na_6Ge_2Se_6$ + $MnCl_2$).

2.3. Powder X-ray diffraction

The laboratory-grade powder X-ray diffraction (PXRD) pattern was obtained using a PANalytical X′Pert Pro diffractometer equipped with a Cu Kα anode and a linear array PIXcel detector over a 2θ range of 5–90° with an average scanning rate of 0.0472° s^{-1}. Hand-ground samples were loaded into an air-tight cell covered with the Kapton film to collect the PXRD pattern. The PXRD pattern of the DMF-washed metathesis route synthesis product is provided in Fig. 1. The experimental PXRD pattern matched very well with the simulated pattern derived from the atomic coordinates of the single-crystal structure solution, indicating phase purity. The finely-ground DMF-washed samples derived from metathesis reactions were used for further characterization and property studies. PXRD of the elemental-route synthesis product is provided in Fig. S2 (Supplementary Materials), which shows presence of a small amount of an unknown impurity. This sample was not used for any property measurement or characterization.

2.4. Differential thermal analysis

Approximately 30 mg of sample was used to collect simultaneous TGA-DSC data on a TA Instruments Q600 SDT from room temperature to 800 °C with a scan rate of 10 °C min^{-1} under an argon atmosphere. The DSC and TGA plots are provided in the Supplementary Materials. The title compound was found to be thermally stable up to 700 °C, after which it shows a melting behavior followed by weight loss, which could be due to selenium loss (Fig. S3).

2.5. Magnetic measurements

The molar magnetic susceptibility measurements of $Na_8Mn_2(Ge_2Se_6)_2$ were carried out with a Quantum Design MPMS SQUID magnetometer while warming in a 2 T applied field from 2 to 300 K under zero-field-cooled and field-cooled (ZFC and FC) conditions. The isothermal magnetization was subsequently measured at 5 and 300 K in varying applied magnetic fields of − 5 to + 5 T.

2.6. Diffuse reflectance UV/Vis/NIR spectroscopy

The optical bandgap was determined from the diffuse reflectance data obtained from a Varian Cary 5000 UV-Vis-NIR spectrophotometer. The specimen was quickly ground, pressed on top of the 100% reflectance standard, $BaSO_4$ (Fisher Scientific, 99.92%), and loaded into the Harrick Praying Mantis accessory. Scans were collected between 2500 and 200 nm at a rate of 600 nm min^{-1}. Wavelength values were converted to energy in electron volts and reflectance data were converted to absorption through the Kubelka-Munk equation [34].

2.7. Attenuated Total Reflectance (ATR) Fourier Transform Infrared (FT-IR) spectroscopy

A Thermo Nicolet 380 FT-IR spectrometer outfitted with an attenuated total reflectance (ATR) accessory was used to collect optical transparency data in the IR region. This setup allows a diamond crystal to be in optical contact with the sample, in this case a microcrystalline powder, resulting in a depth of penetration into the sample that approaches the lower limit of the powder sample particle size, ~2 μm. As a result, the effect of thickness dependence on the intensity of the obtained spectrum is rendered negligible [35]. The spectrum, collected and analyzed with the OMNIC software, consists of 32 scans from 400 cm^{-1} to 4000 cm^{-1}.

2.8. Nonlinear optical (NLO) characterization

Polycrystalline powder of $Na_8Mn_2(Ge_2Se_6)_2$ was provided for NLO characterization. Samples were sieved with size ranges of 20–45 μm, 45–75 μm, 75–90 μm, 90–125 μm, 125–150 μm, and > 150 μm to examine the phase-matching behavior of SHG and THG, laser-induced damage threshold (LIDT) and two-photon absorption (2PA) coefficient β of the sample. Each sample was sealed in a glass capillary tube and mounted on a homemade sample holder. The SHG and THG efficiencies of the sample were compared with an optical-quality reference material, $AgGaSe_2$, obtained from G&H, Cleveland, that was ground to a powder and prepared in the same fashion as the sample under investigation. Note here that the particle size ranges for the reference are slightly different from those for the sample, but this does not affect our determination of the NLO properties.

The series of NLO measurements were carried out at room temperature using the input wavelength (λ = 1800 nm) and intensity (0.67 GW/cm^2). We confirmed that sample damage at this intensity is insignificant. Coherent light with a wavelength of 1064 nm was initially produced using an EKSPLA PL-2250 series diode-pumped Nd:YAG laser with a pulse width, τ, of 30 ps and a repetition rate of 50 Hz to generate tunable pulses. The Nd:YAG laser pumped an EKSPLA Harmonics Unit (HU) H400, in which the input beam was frequency tripled by successive NLO processes of SHG and sum frequency generation (SFG). The beam then entered an EKSPLA PG403-SH-DFG Optical Parametric Oscillator (OPO) composed of four main parts: (i) a double-pass parametric generator, (ii) a single pass parametric amplifier, (iii) a second-harmonic generator (SH), and (iv) a difference frequency generation (DFG) scheme. The output wavelength from the OPO used in our experiments was 1800 nm. This wavelength was deliberately selected in order to ensure that SHG (900 nm) occurs below the bandgap of both the test sample and the reference. This implies that bandgap absorption of SHG can be neglected in the $\chi^{(2)}$ measurement. However, the corresponding THG wavelength is 600 nm, which is above the bandgaps for the title compound and the reference. On the other hand, the LIDT experiment was performed at λ = 1064 nm, which is a typical wavelength for DFG to generate mid-IR radiation. Since both the sample and the reference are optically transparent at 1064 nm, two-photon

absorption (2PA) is the major mechanism for laser-induced damage. The SHG and THG signals were collected using a reflection geometry and a fiber-optic bundle coupled to a spectrometer equipped with a CCD camera. The data collection time was 30 s for SHG and 300 s for THG. A detailed description of our laser and detection setup can be found elsewhere [12].

2.9. Electronic structure calculations

Spin polarized electronic band structure calculations were performed using DFT as implemented in the Vienna ab initio simulation package (VASP) [36–39]. We employed the revised Perdew–Burke–Ernzerhof generalized gradient approximation (PBESol) [40] to the density functional and used Projected Augmented Wave (PAW) pseudopotential to describe the effect of the core electrons with the following states treated as valence states: 4*s* and 4*p* for Se, 4*s* and 4*p* for Ge, 3*p*, 4*s* and 3*d* for Mn, and 3*s* for Na. The kinetic energy cutoff was set to 520 eV and Monkhorst-pack *k*-point grid size of 7 × 4 × 7 was used for Brillouin zone integration [41]. Total energy convergence criterion was set to 10^{-6} eV. The rotationally invariant Hubbard-U type (U = 3 eV) [42] was used to correct the strong correlation of *d* electrons in Mn^{2+} ion. The structure was fully relaxed until the force on each atom was below 0.001 eV/Å.

3. Results and discussion

3.1. Synthesis and crystal structure

Solid-state metathesis stands unique compared to traditional elemental or polychalcogenide flux synthesis in terms of precise product control. Our hypothesis was to replace two sodium ions by a divalent transition metal ion, Mn^{2+}, in $Na_6Ge_2Se_6$ expecting a product in which transition metal ions will covalently connect the preformed ethane-like building units, $[Ge_2Se_6]^{6-}$, to form a layer while the charge balancing Na^+ ions will fill the interlayer space. In this way, one could avoid the formation of several thermodynamically stable binary or ternary phases and form a quaternary phase in which the transition metal preserves its original oxidation state, and the building unit remains intact during the reaction. Fig. 2 shows the solid-state metathesis scheme adopted here with the product retaining the starting building unit and illustrates the mode of connectivity between ethane-like building units $[Ge_2Se_6]^{6-}$ and Mn^{2+} to generate a more predictable composition and structural features.

$Na_8Mn_2(Ge_2Se_6)_2$ crystallizes in polar, NCS space group *C*2, and it is isostructural to $Na_4MgGe_2Se_6$ [13]. The asymmetric unit of $Na_8Mn_2(Ge_2Se_6)_2$ consists of four sodium atoms located on 2*b* and 2*a* Wyckoff sites, one germanium atom and three selenium atoms located on the 4*c* Wyckoff site and one manganese on the 2*a* Wyckoff site (Fig. 3a). The structure of $Na_8Mn_2(Ge_2Se_6)_2$ can be explained in terms of close packing (CP), where the anions form a hexagonal close packing (*hcp*) array in which 5/6th of the octahedral holes are filled by Na and Mn atoms, and the remaining octahedral holes are filled by the Ge–Ge dimer placed parallel to the anion layer (Fig. 3b). Such placement of the Ge–Ge dimer forces Ge to coordinate with the two opposite trigonal faces of the octahedron forming an ethane-like dimer. Considering the standard oxidation state of Na, Mn and Se as +1, +2 and –2, respectively, a formal charge of +6 can be assigned to the [Ge–Ge] unit. In other words, the structure contains ethane-like building units, $[Ge_2Se_6]^{6-}$, connecting the transition metal ions and Na ion forming layers of $[Na(1)Mn(Ge_2Se_6)]^{3-}$. The center of the Ge–Ge bonds is located in octahedral interstitials in the $[Na(1)Mn(Ge_2Se_6)]^{3-}$ layers (Fig. 3c). The $[Na(1)Mn(Ge_2Se_6)]^{3-}$ layers are separated by sodium atoms along the *c*-axis of the unit cell. Manganese and sodium ions adopt distorted octahedral coordination with Mn–Se and Na–Se bond distances in the range of 2.767(3) – 2.837(2) and 2.932(6) – 3.127(6) Å, respectively. Coordination environments of the four sodium atoms are provided in Fig. S4 (Supplementary Materials). The orientation of the Ge–Ge bond (2.402(2) Å) makes an angle of 18.43°(6) with the layer plane, similar to the isostructural $Na_4MgM_2Se_6$ (*M* = Si, Ge). Though several compounds with the general formula $Na_{12-nx}M_x^{n+}(Ge_2Q_6)_2$ (Q = S, Se) have been reported, there exist subtle structural differences among them. Compounds containing trivalent metal ions (M^{3+}) with general formula $Na_9M(Ge_2Q_6)_2$ (M = La^{3+}, Sm^{3+}; Q = S, Se) [24,29] crystallize in a centrosymmetric space group in which rare earth (M^{3+}) and sodium ion occupy the same crystallographic site (25:75), with Ge–Ge bond making an angle of 19.2° with the layer plane. Compounds containing divalent metal ions with general formula $Na_8M_2(Ge_2Q_6)_2$ (M = Eu^{2+}, Pb^{2+}, Sn^{2+}; Q = S, Se) [23,28] also crystallize in a centrosymmetric space group in which M^{2+} and sodium ion occupy the same crystallographic site (50:50) with Ge–Ge bond perpendicular to the layer plane. However, recently reported $Na_4MgGe_2Se_6$ adopts an NCS structure in which the Mg^{2+} ion occupies an independent crystallographic site with the Ge–Ge bond making an angle of 18.54°(3) with the anion layer unlike other M^{2+} compositions. The reported compound $Na_8Mn_2(Ge_2Se_6)_2$ is thus isostructural to the Mg analogue. These subtle structural differences

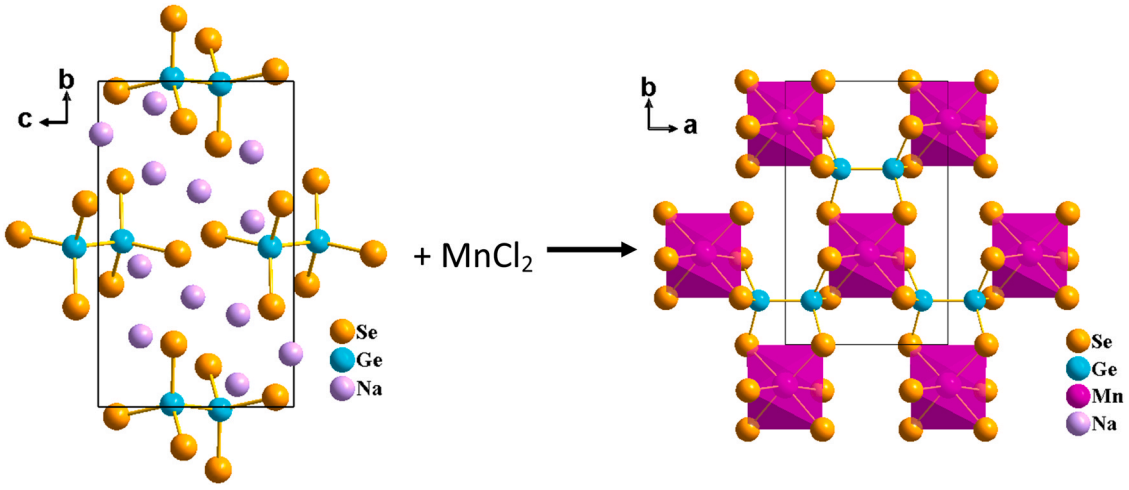

Fig. 2. Schematic representation of the solid-state metathesis reaction, showing the mode of connectivity between ethane-like $[Ge_2Se_6]^{6-}$ units and transition metal Mn^{2+}, leading to the formation of layers in the *ab* plane.

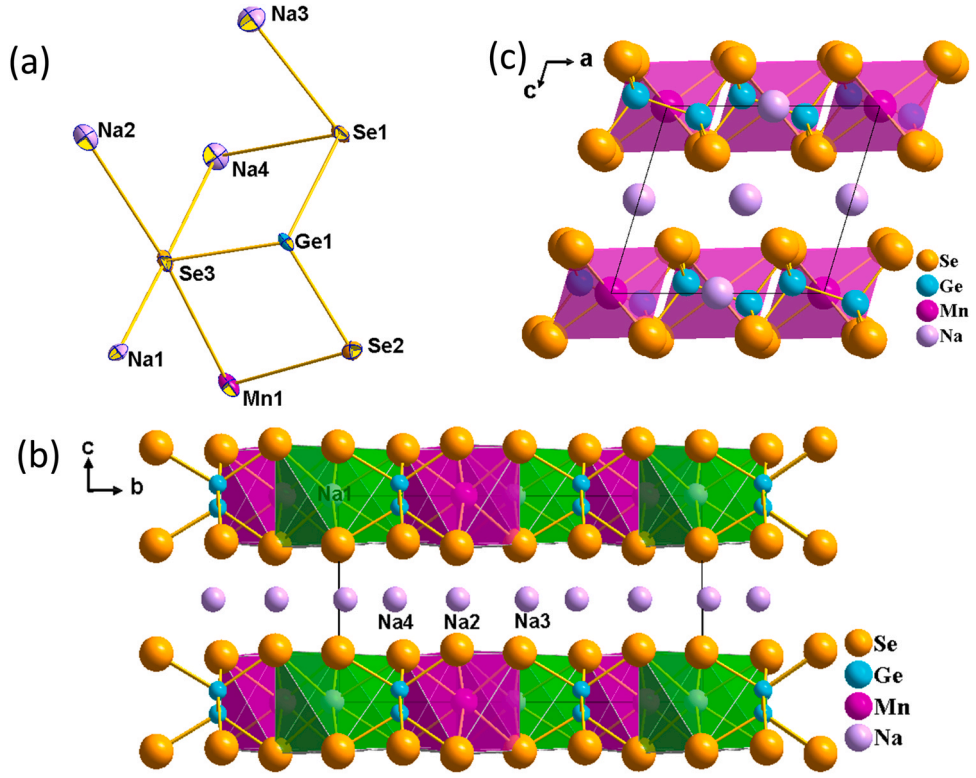

Fig. 3. (a) Asymmetric unit of $Na_8Mn_2(Ge_2Se_6)_2$; (b) View along the *a*-axis showing an *ABAB*-type close packing of anion layers with cations filling octahedral holes; (c) View along the *b*-axis showing the orientation of the Ge–Ge bond with respect to the layer plane.

between the similar compositions could be due to the different ionic radii of the metal cations.

3.2. Magnetic properties

Fig. 4a shows the temperature dependence of magnetic susceptibility and corresponding inverse molar magnetic susceptibility of $Na_8Mn_2(Ge_2Se_6)_2$ in an applied field of 2 T from 2 to 300 K. The asymptotic nature of χ_M vs T plot within the measured temperature range indicates a paramagnetic behavior without any ordering. The temperature dependence of the inverse magnetic susceptibility χ_M^{-1} (T) shows a linear behavior and fitting of the Curie-Weiss law between 200 and 300 K yields a Curie constant of 4.206 emuKmol^{-1} and a Curie-Weiss constant (θ_p) of −23.88 K, respectively. A Curie-Weiss constant (θ_p) with a negative value indicates overall antiferromagnetic (AF) interactions between Mn(II) ions, albeit no sign of any AF ordering up to the lowest temperature measured. The experimental magnetic moment per manganese derived from the Curie constant is 5.8 μ_B, which is very close to the spin-only magnetic moment of 5.92 μ_B for high spin Mn^{2+} with five unpaired *d* electrons. The variable field isothermal magnetization measured at 300 K shows a sluggish increase in the magnetization to a value of 0.11 Nμ_B at 5 T, whereas at 3 K, the magnetization gradually increases up to 2.86 Nμ_B, giving ~60% of the theoretical saturation moment (5 Nμ_B) for high spin Mn^{2+} (Fig. 4b).

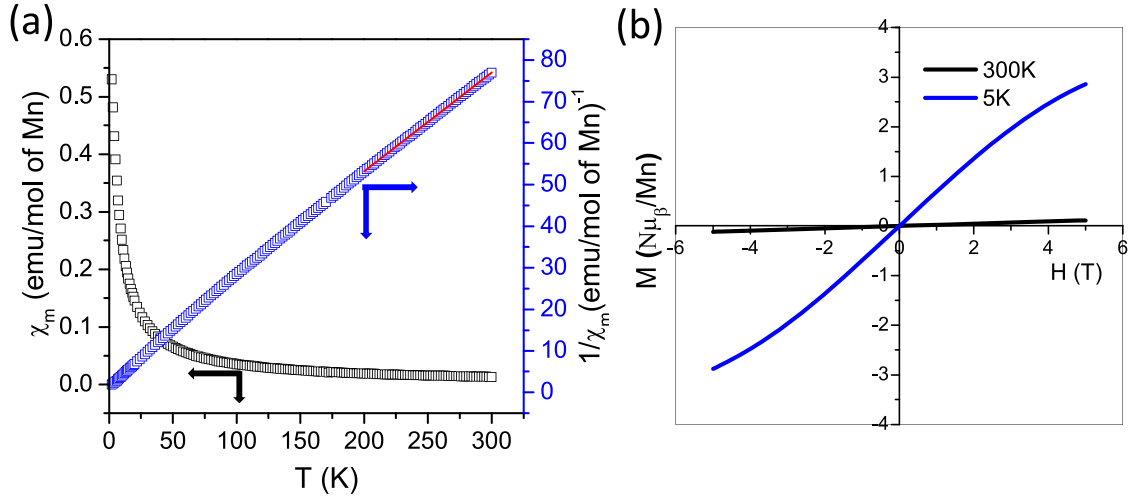

Fig. 4. (a) Temperature-dependent molar and inverse molar magnetic susceptibility of $Na_8Mn_2(Ge_2Se_6)_2$ acquired at an applied field of 2 T. The red line indicates linear fitting of the data. (b) Isothermal *M–H* scans at 5 and 300 K. (For interpretation of the references to colour in this figure legend, the reader is referred to the web version of this article.)

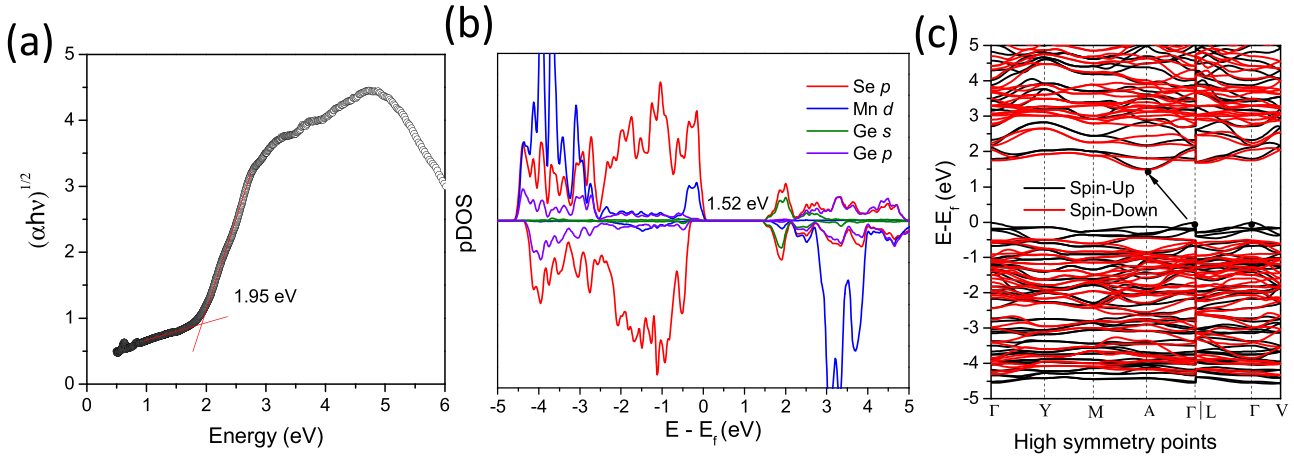

Fig. 5. (a) Absorption vs photon energy constructed from the diffuse reflectance UV-Vis-NIR data of $Na_8Mn_2(Ge_2Se_6)_2$; (b) Partial density of states of $Na_8Mn_2(Ge_2Se_6)_2$ calculated using DFT + U by applying U = 3 eV; (c) Electronic band structure of $Na_8Mn_2(Ge_2Se_6)_2$.

3.3. Optical bandgap and band structure analysis

Diffuse reflectance measurements were performed on an as-synthesized, powder sample of $Na_8Mn_2(Ge_2Se_6)_2$. The equation $\alpha h\nu = A(h\nu - E_g)^m$ was employed to estimate the optical bandgap, where α is the absorption coefficient (Kubelka–Munk function), $h\nu$ is the photon energy, and $m = 1/2$ and 2 depending on whether the transition is direct or indirect, respectively. $Na_8Mn_2(Ge_2Se_6)_2$ exhibits linearity in the $h\nu$ vs. $(\alpha h\nu)^{1/2}$ plot suggesting an indirect nature of the bandgap with a value of 1.95 eV (Fig. 5a).

In order to understand the origin of bandgap and the contribution of orbitals to the Fermi level, spin polarized electronic band structure calculations at the DFT level were carried out. Because of the presence of localized *d* electrons, an additional Hubbard-like term with simplified Dudarev approach $U_{eff} = U - J = 3$ eV, was used for Mn 3*d* orbitals. Fig. 5b displays the partial density of states (pDOS) with a bandgap of 1.52 eV. This value is in reasonable agreement, i.e. expectedly underestimated, with the experimental bandgap of 1.95 eV obtained through diffuse reflectance spectroscopy (DRS) measurements. The pDOS shows that the states at the top of the valence band have major contributions from Se *p* orbitals and Mn *d* orbitals, whereas the bottom of the conduction band has major contributions from Se *p* orbitals and Ge *s* orbitals. Band dispersion along the high symmetry points in the Brillouin zone is provided in Fig. 5c. The band dispersion shows the indirect nature of the bandgap, which agrees well with the experimental DRS measurements. The top of the valence band occurs at the Γ point and the bottom of the conduction band occurs at the A point of the Brillouin zone. Note that in the isostructural $Na_4MgGe_2Se_6$, the contribution from Mg to the top of the valence band is not very significant. This suggests predominant ionic interactions between Mg and Se, thus resulting in a wider bandgap of 2.53 eV compared to $Na_8Mn_2(Ge_2Se_6)_2$ which has the bandgap of 1.95 eV as the Mn *d* orbitals have significant overlap with the Se *p* orbitals and that raises the Fermi level [13]. Therefore, substitution with other M^{+2} metals for Mn could further tune the bandgap of this compound.

3.4. Optical transparency

ATR FT-IR spectroscopy of a microcrystalline specimen of the title compound was used to gain a preliminary assessment of the window of optical clarity. $Na_8Mn_2(Ge_2Se_6)_2$ exhibits a potentially wide region of optical transparency throughout the measured range of 2.5–25 μm (Fig. 6). A more accurate assessment of the transparency can only be determined on a high-quality, sizeable single crystal specimen. As

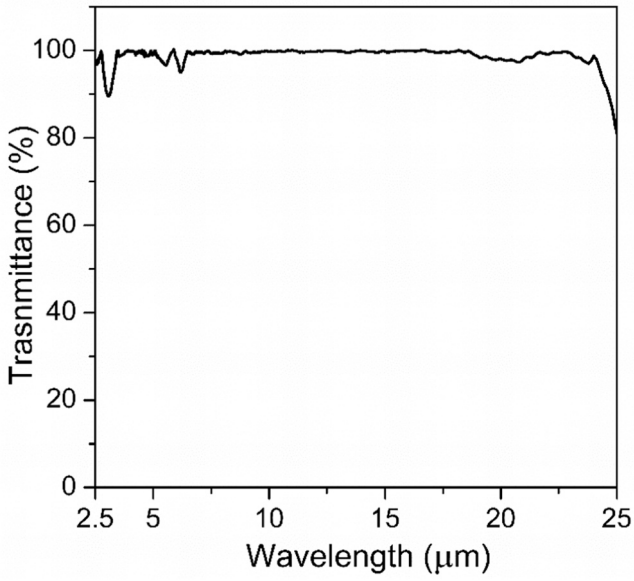

Fig. 6. Transmittance (%) from 2.5 μm to 25 μm for $Na_8Mn_2(Ge_2Se_6)_2$.

generally expected for chalcogenides, the IR transparency is theoretically high and extremely attractive.

3.5. Second and Third Harmonic Generation (SHG and THG)

A plot of the SHG counts of the sample (red) and the reference (black) as a function of particle size range for λ = 1800 nm is shown in Fig. 7a. The compound is non-phase matchable, as the measured SHG counts decrease with increasing particle size, although there are some oscillatory behaviors in the middle sizes due to the phase-matching factor of a sinc function squared [43]. The second-order susceptibility of the sample, $\chi_S^{(2)}$, was compared with that of AgGaSe$_2$ using the Kurtz powder method [12,43] for the non-phase-matching case;

$$\chi_S^{(2)} = \chi_R^{(2)} \frac{l_R}{l_S} \left(\frac{I_S^{SHG}}{I_R^{SHG}} \right)^{1/2}, \quad (1)$$

where I_S^{SHG} and I_R^{SHG} are the measured SHG counts from the sample and the reference and l_S and l_R are the experimentally estimated SHG coherence lengths of the sample and reference, which are 60 and 32.5 μm, respectively. Using $\chi_R^{(2)} \sim$ 66 pm/V for $AgGaSe_2$ [16], our

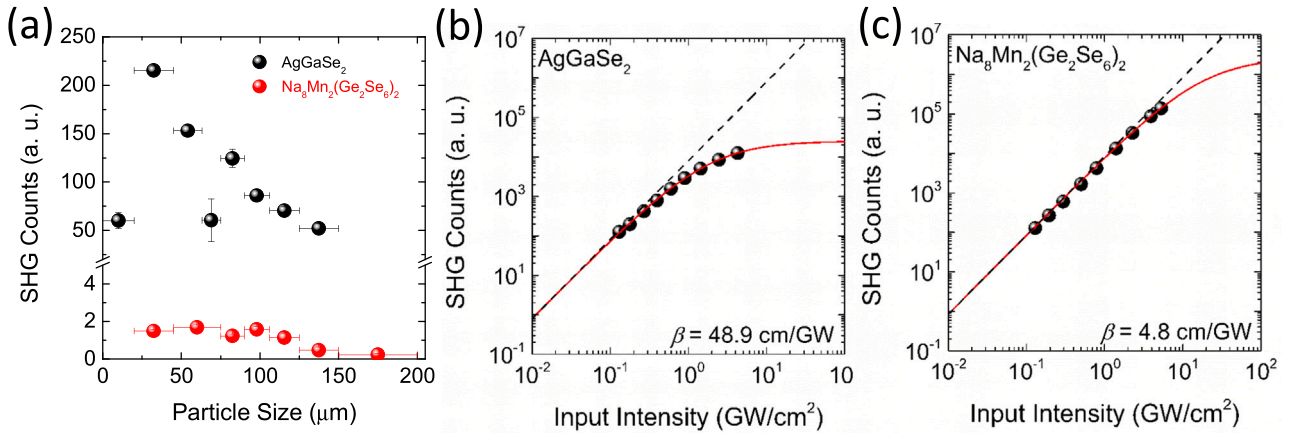

Fig. 7. (a) Particle size dependence of SHG for $AgGaSe_2$ (black) and $Na_8Mn_2(Ge_2Se_6)_2$ (red) at λ = 1800 nm. Logarithmic plots of the SHG counts versus input laser intensity for (b) $AgGaSe_2$ and (c) $Na_8Mn_2(Ge_2Se_6)_2$ for I = 0.1–10 GW/cm^2 at λ = 1064 nm and τ = 30 ps. The red curve in each case indicates the best fit using Eq. (2). The black dashed line corresponds to the case for no optical damage, when $\beta = 0$. (For interpretation of the references to colour in this figure legend, the reader is referred to the web version of this article.)

calculation yields $\chi_S^{(2)}(Na_8Mn_2(Ge_2Se_6)_2)$ ~ 3.2 ± 0.3 pm/V at 1800 nm.

In order to assess the LIDT, the SHG counts of $AgGaSe_2$ and $Na_8Mn_2(Ge_2Se_6)_2$ of the powder diameter d = 106 – 125 μm were measured as a function of input laser intensity at 1064 nm (Fig. 7b and c). $AgGaSe_2$ and $Na_8Mn_2(Ge_2Se_6)_2$ are both 2PA active at this excitation wavelength. Note here that a lower β value corresponds to a higher LIDT. The SHG counts, measured as a function of input intensity, are expected to increase according to the square power law as given by

$$I_{SHG} = a\left(\frac{I}{1+\beta dI}\right)^2, \quad (2)$$

where I is the fundamental intensity, I_{SHG} is the SHG intensity, β is the 2PA coefficient, d is the particle size of the microcrystalline powder, and a is a proportionality constant that incorporates $\chi^{(2)}$. We estimated the LIDT as the intensity in which the data (dots) deviate from the black dashed line in Fig. 7b and c. Accordingly, the LIDT and β of $AgGaSe_2$ are 0.2 GW/cm^2 and 48.9 cm/GW and those of $Na_8Mn_2(Ge_2Se_6)_2$ are 1.8 GW/cm^2 and 4.8 cm/GW, respectively.

Although the second-order nonlinearity of the sample is small, it is notable that the title compound is less prone to optical damage, which may be due to its wider bandgap compared with that of the reference. The figure of merit (FOM) for the SHG performance can be defined by $|\chi^{(2)}|^2/\beta$. The corresponding values, including $\chi^{(2)}$, β, LIDT and FOM for the sample and reference are listed in Table 3.

Lastly, the THG responses of $Na_8Mn_2(Ge_2Se_6)_2$ and $AgGaSe_2$ were examined using the smallest particle size with an incident wavelength of λ = 1800 nm (Fig. 8), because it is quite certain that both sample and reference would exhibit non-phase-matching THG with a larger phase mismatch between the fundamental frequency and the THG frequency, compared with the case for SHG. Note here that THG radiation would be efficiently absorbed by both sample and reference because the corresponding THG photon energy is about 2.07 eV (600 nm in wavelength) that is above their bandgaps.

Table 3
Comparison of NLO properties of the sample and the reference.

	$AgGaSe_2$	$Na_8Mn_2(Ge_2Se_6)_2$
$\chi^{(2)}$ (pm/V) (λ = 1800 nm)	66	3.2 ± 0.3
β (cm/GW) (λ = 1064 nm)	48.9	4.8
LIDT(GW/cm^2) (λ = 1064 nm; τ = 30 ps)	0.2	1.8
FOM	89.1	2.1 ± 1.0

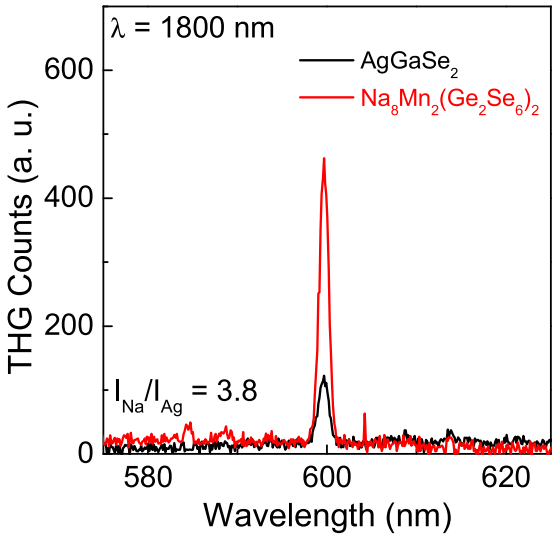

Fig. 8. THG measurements of $AgGaSe_2$ (black) and $Na_8Mn_2(Ge_2Se_6)_2$ (red). (For interpretation of the references to colour in this figure legend, the reader is referred to the web version of this article.)

Typically, a good SHG material also exhibits a good THG response. Therefore, it is rather surprising that the THG counts from the sample are about 3.8 times larger than those from the reference, although this could arise partly from more severe THG absorption by the reference having a smaller bandgap of 1.80 eV.

The $\chi_S^{(3)}$ value for $Na_8Mn_2(Ge_2Se_6)_2$ was calculated from the experimentally measured THG counts from the sample (I_S^{THG}) and the reference (I_R^{THG}) by using

$$\chi_S^{(3)} = \chi_R^{(3)}\left(\frac{I_S^{THG}}{I_R^{THG}}\right)^{1/2} \quad (3)$$

where $\chi_R^{(3)}$ is about 1.6×10^5 pm^2/V^2 [7] and the THG coherence lengths, being much smaller than our smallest sieve size, are assumed to be same for simplicity. Eq. (3) yields $\chi_S^{(3)}$ ~3.0×10^5 pm^2/V^2 at 1800 nm for our sample. This value could be somewhat overestimated, but our initial assessment clearly indicates that $Na_8Mn_2(Ge_2Se_6)_2$ is a good candidate material for various applications utilizing the third-order nonlinearity.

4. Conclusions

A new polar, paramagnetic semiconductor compound, $Na_8Mn_2(Ge_2Se_6)_2$, was synthesized. $Na_8Mn_2(Ge_2Se_6)_2$ shows high LIDT (9x $AgGaSe_2$) and modest SHG response. More importantly, THG measurements indicate that $Na_8Mn_2(Ge_2Se_6)_2$ shows a strong THG response at 1800 nm. The observed NLO properties of the title compound are rather unusual, exhibiting a modest $\chi^{(2)}$ and an excellent $\chi^{(3)}$, which needs more investigation in the future. Although $Na_8Mn_2(Ge_2Se_6)_2$ is less attractive in terms of SHG efficiency at this moment, it is believed that there are avenues to improve the NLO properties by systematic derivatization of the constituent elements to induce larger dipole moments. High LIDT, modest SHG, and strong THG response along with potentially wide IR transmission range make the title compound a promising candidate for various IR NLO applications.

CRediT authorship contribution statement

Srikanth Balijapelly: Formal analysis, Investigation, Validation, Visualization, and Writing-Original Draft. **Andrew J. Craig:** Formal analysis, Visualization, Writing-Review & Editing. **Jeong Bin Cho:** Investigation, Visualization. Joon I. Jang: Investigation, Supervision, Funding acquisition, and Writing-Review & Editing. **Kartik Ghosh:** Investigation. Jennifer A. Aitken: Resources, Supervision, Writing-Review & Editing. **Aleksandr V. Chernatynskiy:** Supervision. **Amitava Choudhury:** Conceptualization, Supervision, Validation, Resources, Writing-Review & Editing, and Funding acquisition.

Declaration of Competing Interest

The authors declare that they have no known competing financial interests or personal relationships that could have appeared to influence the work reported in this paper.

Acknowledgements

The authors, AC, AVC and SB, thank NSF, USA (grant No. DMR-1809128) for the funding of this project. The authors JAA and AJC acknowledge the support of the United States National Science Foundation, Division of Materials Research, under grant number DMR-1611198. J.I.J. acknowledges the support by the Basic Science Research Program 2021R1A2C2013625 through the National Research Foundation of Korea (NRF), funded by the Korean government.

Appendix A. Supporting information

Supplementary data associated with this article can be found in the online version at doi:10.1016/j.jallcom.2021.163392.

References

[1] B.J. Eggleton, B. Luther-Davies, K. Richardson, Chalcogenide photonics, Nat. Photon. 5 (2011) 141–148, https://doi.org/10.1038/nphoton.2011.309
[2] I. Chung, M.G. Kanatzidis, Metal Chalcogenides: a rich source of nonlinear optical materials, Chem. Mater. 26 (2013) 849–869, https://doi.org/10.1021/CM401737S
[3] X. Luo, Z. Li, Y. Guo, J. Yao, Y. Wu, Recent progress on new infrared nonlinear optical materials with application prospect, J. Solid State Chem. 270 (2019) 674–687, https://doi.org/10.1016/j.jssc.2018.12.036
[4] V.A. Serebryakov, É.V. Boïko, N.N. Petrishchev, A.V. Yan, Medical applications of mid-IR lasers. Problems and prospects, J. Opt. Technol. 77 (2010) 6–17, https://doi.org/10.1364/JOT.77.000006
[5] A.S. Haynes, F.O. Saouma, C.O. Otieno, D.J. Clark, D.P. Shoemaker, J.I. Jang, M.G. Kanatzidis, Phase-change behavior and nonlinear optical second and third harmonic generation of the one-dimensional $K_{(1-x)}Cs_xPSe_6$ and metastable β-$CsPSe_6$, Chem. Mater. 27 (2015) 1837–1846, https://doi.org/10.1021/acs.chemmater.5b00065
[6] A.S. Haynes, A. Banerjee, F.O. Saouma, C.O. Otieno, J.I. Jang, M.G. Kanatzidis, Phase transition, conformational exchange, and nonlinear optical third harmonic generation of $ACsP_2Se_8$ (A = K, Rb, Cs), Chem. Mater. 28 (2016) 2374–2383, https://doi.org/10.1021/acs.chemmater.6b00551
[7] D. Friedrich, H.R. Byun, S. Hao, S. Patel, C. Wolverton, J.I. Jang, M.G. Kanatzidis, Layered and cubic semiconductors $AGaM'Q4$ ($A^+ = K^+$, Rb^+, Cs^+, Tl^+; $M'^{4+} = Ge^{4+}$, Sn^{4+}; $Q^{2-} = S^{2-}$, Se^{2-}) and high third-harmonic generation, J. Am. Chem. Soc. 142 (2020) 17730–17742, https://doi.org/10.1021/jacs.0c08638
[8] Y. Kim, I. Seo, S.W. Martin, J. Baek, P. Shiv Halasyamani, N. Arumugam, H. Steinfink, Characterization of new infrared nonlinear optical material with high laser damage threshold, $Li_2Ga_2GeS_6$, Chem. Mater. 20 (2008) 6048–6052, https://doi.org/10.1021/cm8007304
[9] W. Yin, K. Feng, W. Hao, J. Yao, Y. Wu, Synthesis, structure, and properties of $Li_2In_2MQ_6$ (M = Si, Ge; Q = S, Se): a new series of ir nonlinear optical materials, Inorg. Chem. 51 (2012) 5839–5843, https://doi.org/10.1021/ic300373z
[10] J.A. Brant, D.J. Clark, Y.S. Kim, J.I. Jang, J.-H. Zhang, J.A. Aitken, $Li_2CdGeS4$, A diamond-like semiconductor with strong second order optical nonlinearity in the infrared and exceptional laser damage threshold, Chem. Mater. 26 (2014) 3045–3048, https://doi.org/10.1021/cm501029s
[11] J.I. Jang, D.J. Clark, J.A. Brant, J.A. Aitken, Y.S. Kim, Highly efficient infrared optical nonlinearity of a wide-bandgap chalcogenide Li_2CdGeS_4, Opt. Lett. 39 (2014) 4579–4582, https://doi.org/10.1364/OL.39.004579
[12] J.A. Brant, D.J. Clark, Y.S. Kim, J.I. Jang, A. Weiland, J.A. Aitken, Outstanding laser damage threshold in Li_2MnGeS_4 and tunable optical nonlinearity in diamond-like semiconductors, Inorg. Chem. 54 (2015) 2809–2819, https://doi.org/10.1021/IC502981R
[13] K. Wu, Z. Yang, S. Pan, $Na_4MgM_2Se_6$ (M = Si, Ge): the first noncentrosymmetric compounds with special ethane-like $[M_2Se_6]^{6-}$ units exhibiting large laser-damage thresholds, Inorg. Chem. 54 (2015) 10108–10110, https://doi.org/10.1021/acs.inorgchem.5b01859
[14] K. Wu, Z. Yang, S. Pan, Na_2BaMQ_4 (M = Ge, Sn; Q = S, Se): Infrared nonlinear optical materials with excellent performances and that undergo structural transformations, Angew. Chem. Int. Ed. 55 (2016) 6713–6715, https://doi.org/10.1002/anie.201602317
[15] M.L. Zhou, L. Kang, J.Y. Yao, Z.S. Lin, Y.C. Wu, C.T. Chen, Midinfrared nonlinear optical thiophosphates from $LiZnPS_4$ to $AgZnPS_4$: a combined experimental and theoretical study, Inorg. Chem. 55 (2016) 3724–3726, https://doi.org/10.1021/acs.inorgchem.6b00517
[16] J.-H. Zhang, D.J. Clark, J.A. Brant, K.A. Rosmus, P. Grima, J.W. Lekse, J.I. Jang, J.A. Aitken, α-Li_2ZnGeS_4: a wide-bandgap diamond-like semiconductor with excellent balance between laser-induced damage threshold and second harmonic generation response, Chem. Mater. 32 (2020) 8947–8955, https://doi.org/10.1021/acs.chemmater.0c02929
[17] A. Abudurusuli, J.B. Huang, P. Wang, Z.H. Yang, S.L. Pan, J.J. Li, $Li_4MgGe_2S_7$: the first alkali and alkaline-earth diamond-like infrared nonlinear optical material with exceptional large band gap, Angew. Chem. Int. Ed. 60 (2021) 24131–24136, https://doi.org/10.1002/anie.202107613
[18] K.O. Klepp, Darstellung und Kristallstruktur von Na_4GeSe_4: ein neues ortho-Selenogermanat(IV), Z. Naturforsch. B 40 (1985) 878–882, https://doi.org/10.1515/ZNB-1985-0705
[19] B. Eisenmann, J. Hansa, H. Schaefer, $Na_6Ge_2Se_7$, das erste Selenidosorogermanat (IV), Rev. Chim. Minar. 23 (1986) 8–13.
[20] B. Eisenmann, J. Hansa Z, Crystal structure of tetrapotassium hexaselenodigermanate, $K_4Ge_2Se_6$, Z. Krist. Cryst. Mater. 203 (1993) 301–302, https://doi.org/10.1524/zkri.1993.203.12.301
[21] B. Eisenmann, E. Kieselbach, H. Schäfer, H. Schrod, Über Thio-, Selenido- und Telluridogermanate (III): Zur Kenntnis von $K_6Ge_2S_6$, $K_6Ge_2Se_6$ und $Na_6Ge_2Te_6$, Z. Anorg. Allg. Chem. 516 (1984) 49–54, https://doi.org/10.1002/ZAAC.19845160908
[22] B. Eisenmann, J. Hansa, U.H. Schäfer, Oligoselenidogermanate (III): Zur kenntnis von $Na_6Ge_2Se_6$ und $Na_8Ge_4Se_{10}$, Mater. Res. Bull. 20 (1985) 1339–1346, https://doi.org/10.1016/0025-5408(85)90127-8
[23] G.A. Marking, M.G. Kanatzidis, The ethane-like $[Ge_2S_6]$ metals in $Na_8Pb_2[Ge_2S_6]_2$, $Na_8Sn_2[Ge_2S_6]_2$, and $Na_8Pb_2[Si_2Se_6]_2$, J. Alloy. Compd. 259 (1997) 122–128, https://doi.org/10.1016/S0925-8388(97)00038-8
[24] B.R. Martin, L.A. Polyakova, P.K. Dorhout, Synthesis and characterization of a family of two related quaternary selenides: $Na_8Eu_2(Si_2Se_6)$ 2 and $Na_9Sm(Ge_2Se_6)_2$, J. Alloy. Compd. 408–412 (2006) 490–495, https://doi.org/10.1016/j.jallcom.2004.12.091
[25] A. Choudhury, L.A. Polyakova, I. Hartenbach, T. Schleid, P.K. Dorhout, Synthesis, structures, and properties of layered quaternary chalcogenides of the general formula $ALnEQ_4$ (A = K, Rb; Ln = Ce, Pr, Eu; E = Si, Ge; Q = S, Se), Z. Anorg. Allg. Chem. 632 (2006) 2395–2401, https://doi.org/10.1002/ZAAC.200600226
[26] A. Choudhury, L.A. Polyakova, S. Strobel, P.K. Dorhout, Two non-centrosymmetric cubic seleno-germanates related to CsCl-type structure: Synthesis, structure, magnetic and optical properties, J. Solid State Chem. 180 (2007) 1381–1389, https://doi.org/10.1016/j.jssc.2007.02.002
[27] A. Choudhury, S. Strobel, B.R. Martin, A.L. Karst, P.K. Dorhout, Synthesis of a family of solids through the building-block approach: a case study with Ag+ substitution in the ternary Na-Ge-Se system, Inorg. Chem. 46 (2007) 2017–2027, https://doi.org/10.1021/ic061064z
[28] A. Choudhury, K. Ghosh, F. Grandjean, G.J. Long, P.K. Dorhout, Structural, optical, and magnetic properties of $Na_8Eu_2(Si_2S_6)_2$ and $Na_8Eu_2(Ge_2S_6)_2$: Europium(II) quaternary chalcogenides that contain an ethane-like $(Si_2S_6)^{6-}$ or $(Ge_2S_6)^{6-}$ moiety, J. Solid State Chem. 226 (2015) 74–80, https://doi.org/10.1016/j.jssc.2015.02.006
[29] B.R. Martin, J.M. Knaust, P.K. Dorhout, Crystal structure of nonasodium lanthanum(III) bis[hexaselenodigermanate], $Na_9La[Ge_2Se_6]_2$, Z. Krist. New Cryst. Struct. 220 (2005), https://doi.org/10.1524/ncrs.2005.220.3.294 294–294.

[30] Bruker- SMART. Bruker AXS Inc., Madison, Wisconsin, USA, (2002).
[31] Bruker-SAINT and SADABS, and SHELXTL. Bruker AXS Inc., Madison, Wisconsin, USA, (2008).
[32] G.M. Sheldrick, A short history of SHELX, Acta Crystallogr. Sect. A Found. Crystallogr 64 (2008) 112–122, https://doi.org/10.1107/S0108767307043930
[33] C.B. Hübschle, G.M. Sheldrick, B. Dittrich, ShelXle: a Qt Graphical user interface for SHELXL, J. Appl. Crystallogr. 44 (2011) 1281–1284, https://doi.org/10.1107/s0021889811043202
[34] P. Kubelka, F. Munk, Ein Beitrag Zur Optik Der Farbanstriche, Z. Techn. Phys. 12 (1931) 593–601.
[35] R.J. McGowan, Attenuated total reflectance vs. Transmission infrared spectrometry in the quantitative evaluation of paint vehicles, Anal. Chem. 35 (1963) 1664–1665, https://doi.org/10.1021/ac60204a037
[36] G. Kresse, J. Hafner, Ab initio molecular dynamics for liquid metals, Phys. Rev. B 47 (1993) 558–561, https://doi.org/10.1103/PhysRevB.47.558
[37] G. Kresse, J. Furthmüller, Efficiency of ab-initio total energy calculations for metals and semiconductors using a plane-wave basis set, Comput. Mater. Sci. 6 (1996) 15–50, https://doi.org/10.1016/0927-0256(96)00008-0
[38] G. Kresse, J. Furthmüller, Efficient iterative schemes for ab initio total-energy calculations using a plane-wave basis set, Phys. Rev. B 54 (1996) 11169–11186, https://doi.org/10.1103/PhysRevB.54.11169
[39] D. Joubert, From ultrasoft pseudopotentials to the projector augmented-wave method, Phys. Rev. B 59 (1999) 1758–1775, https://doi.org/10.1103/PhysRevB.59.1758
[40] J.P. Perdew, A. Ruzsinszky, G.I. Csonka, O.A. Vydrov, G.E. Scuseria, L.A. Constantin, X. Zhou, K. Burke, Restoring the density-gradient expansion for exchange in solids and surfaces, Phys. Rev. Lett. 100 (2008) 136406, https://doi.org/10.1103/PhysRevLett.100.136406
[41] H.J. Monkhorst, J.D. Pack, Special points for brillonin-zone integrations, Phys. Rev. B. 13 (1976) 5188–5192, https://doi.org/10.1103/PhysRevB.13.5188
[42] A.I. Liechtenstein, V.I. Anisimov, J. Zaanen, Density-functional theory and strong interactions: orbital ordering in mott-hubbard insulators, Phys. Rev. B. 52 (1995) R5467–R5470, https://doi.org/10.1103/PhysRevB.52.R5467
[43] S.K. Kurtz, T.T. Perry, A powder technique for the evaluation of nonlinear optical materials, J. Appl. Phys. 39 (2003) 3798–3813, https://doi.org/10.1063/1.1656857